

Braking of tearing mode rotation by ferromagnetic conducting walls in tokamaks

Richard Fitzpatrick

Citation: *Physics of Plasmas* **22**, 092506 (2015); doi: 10.1063/1.4930267

View online: <http://dx.doi.org/10.1063/1.4930267>

View Table of Contents: <http://scitation.aip.org/content/aip/journal/pop/22/9?ver=pdfcov>

Published by the [AIP Publishing](#)

Articles you may be interested in

[Phase locking of multi-helicity neoclassical tearing modes in tokamak plasmas](#)

Phys. Plasmas **22**, 042514 (2015); 10.1063/1.4919030

[Roles of poloidal rotation in the \$q=1\$ high-order harmonic tearing modes in a tokamak plasma](#)

Phys. Plasmas **20**, 012512 (2013); 10.1063/1.4789381

[Nonlinear dynamics of rotating drift-tearing modes in tokamak plasmas](#)

Phys. Plasmas **15**, 092506 (2008); 10.1063/1.2980286

[Hypersonic drift-tearing magnetic islands in tokamak plasmas](#)

Phys. Plasmas **14**, 122502 (2007); 10.1063/1.2811928

[Bifurcation of generic metastable tearing modes interacting with resonant magnetic fields](#)

Phys. Plasmas **11**, 1440 (2004); 10.1063/1.1649992



PFEIFFER VACUUM

VACUUM SOLUTIONS FROM A SINGLE SOURCE

Pfeiffer Vacuum stands for innovative and custom vacuum solutions worldwide, technological perfection, competent advice and reliable service.



125 YEARS
NOTHING IS BETTER

Braking of tearing mode rotation by ferromagnetic conducting walls in tokamaks

Richard Fitzpatrick

Institute for Fusion Studies, University of Texas at Austin, Austin, Texas 78712-1203, USA

(Received 23 June 2015; accepted 21 August 2015; published online 10 September 2015)

An in-depth investigation of the braking of tearing mode rotation in tokamak plasmas via eddy currents induced in external ferromagnetic conducting structures is performed. In general, there is a “forbidden band” of tearing mode rotation frequencies that separates a branch of high-frequency solutions from a branch of low-frequency solutions. When a high-frequency solution crosses the upper boundary of the forbidden band, there is a bifurcation to a low-frequency solution, and vice versa. The bifurcation thresholds predicted by simple torque-balance theory (which takes into account the electromagnetic braking torque acting on the plasma, as well as the plasma viscous restoring torque, but neglects plasma inertia) are found to be essentially the same as those predicted by more complicated time-dependent mode braking theory (which takes inertia into account). Significant ferromagnetism causes otherwise electromagnetically thin conducting structures to become electromagnetically thick and also markedly decreases the critical tearing mode amplitude above which the mode “locks” to the conducting structures (i.e., the high-frequency to low-frequency bifurcation is triggered). On the other hand, if the ferromagnetism becomes too large, then the forbidden band of mode rotation frequencies is suppressed, and the mode frequency consequently varies smoothly and reversibly with the mode amplitude. © 2015 AIP Publishing LLC.

[<http://dx.doi.org/10.1063/1.4930267>]

I. INTRODUCTION

A tokamak is a device whose purpose is to confine a high-temperature plasma on a set of nested toroidal magnetic flux-surfaces.¹ Charged particles are free to circulate rapidly around the flux-surfaces, but can only diffuse slowly across them, as a consequence of their relatively small gyroradii.

Tokamak plasmas are subject to a number of macroscopic instabilities that limit their effectiveness. Such instabilities can be divided into two broad classes. So-called *ideal instabilities* are non-reconnecting modes that disrupt the plasma in a matter of microseconds.² However, such instabilities can usually be avoided by limiting the plasma pressure and/or by tailoring the toroidal current profile.³ *Tearing modes*, on the other hand, are relatively slowly growing instabilities that are more difficult to prevent.^{3,4} These instabilities tend to saturate at relatively low levels,^{5–8} in the process reconnecting magnetic flux-surfaces to form helical structures known as *magnetic islands*. Magnetic islands are radially localized structures centered on so-called rational flux-surfaces that satisfy $\mathbf{k} \cdot \mathbf{B} = 0$, where \mathbf{k} is the wave vector of the instability, and \mathbf{B} the equilibrium magnetic field. Magnetic islands degrade plasma confinement because they enable heat and particles to flow very rapidly along field-lines from their inner to their outer radii, implying an almost complete loss of confinement in the region lying between these radii.⁹

Toroidal plasma rotation plays an important, and in some cases a critical, role in tokamaks. One reason for this is that, with sufficiently fast rotation, magnetic islands co-rotate with the plasma at their associated rational surfaces.¹⁰ However, if the plasma rotation becomes too small, then

such islands can lock (i.e., become stationary in the laboratory frame of reference).^{10–15} Mode locking has a variety of negative consequences. In particular, locking often results in a disruption (i.e., a total loss of plasma containment).^{16,17}

Mode locking usually takes place in two distinct stages.¹⁰ First, the island rotation frequency is reduced to a small fraction of its unperturbed value via electromagnetic torques associated with eddy currents induced in the conducting structures that inevitably surround the plasma. Typical examples of such structures include the vacuum vessel and passive plates used to stabilize kink modes. Henceforth, these structures are simply referred to as the “wall.” Second, the island locks to a static resonant error-field. (Such fields are always present in tokamak plasmas due to magnetic field-coil misalignments, poorly compensated coil feeds, etc.) Generally speaking, unless the error-field in question is unusually large, mode locking is not possible without the prior braking action of wall eddy currents.

A theory of tearing mode rotation braking due to eddy currents excited in the wall was developed by Nave and Wesson.¹³ According to this theory, the electromagnetic braking torque acting on the island is balanced by plasma inertia (because a significant fraction of the plasma is forced to co-rotate with the island as a consequence of the inability of the plasma to easily cross the island’s magnetic separatrix, as well as the action of plasma perpendicular viscosity). In Nave and Wesson’s theory, the island rotation frequency decelerates smoothly and reversibly as the island width increases. An alternative theory was subsequently developed by Fitzpatrick in which the electromagnetic braking torque is balanced by plasma viscosity, and plasma inertia plays a negligible role.¹⁰ Nave and Wesson’s theory is appropriate

to islands that grow comparatively rapidly, i.e., on a timescale that is small compared to the plasma momentum confinement time. Fitzpatrick's theory, on the other hand, is appropriate to islands that grow comparatively slowly: i.e., on a timescale that is long compared to the momentum confinement time. According to Fitzpatrick's theory, if the intrinsic plasma rotation at the rational surface is sufficiently large, then there is a "forbidden band" of island rotation frequencies. This band (which has been directly observed experimentally¹⁸) separates a branch of high-frequency solutions from a branch of low-frequency solutions. If the island width becomes sufficiently large that a high-frequency solution crosses the upper boundary of the forbidden band, then there is a bifurcation to a low-frequency solution. This bifurcation is associated with a sudden collapse in the island rotation frequency to a comparatively low level. Such a collapse is almost certain to lead to mode locking.

Fitzpatrick's theory of tearing mode rotation braking is based on the hypothesis that solutions of the steady-state torque balance equation (the two torques in question being the electromagnetic braking torque and the viscous restoring torque) for which the island rotation frequency decreases with increasing island width are dynamically stable, whereas solutions for which the island frequency increases with increasing island width are dynamically unstable. The first aim of this paper is to explicitly test this hypothesis by comparing the predictions of simple torque-balance theory with those of the more complicated time-dependent mode braking equations (which take plasma inertia into account).

For the sake of simplicity, Fitzpatrick's theory of wall-induced tearing mode rotation braking assumes that the wall is electromagnetically thin (i.e., that the radial thickness of the wall is much less than the electromagnetic skin-depth in the wall material). This assumption is reasonable for present-day tokamaks, which tend to have relatively thin walls, but is not appropriate to next-step devices, such as ITER,¹⁹ which will necessarily have thick walls (for engineering reasons). Thus, the second aim of this paper is to generalize Fitzpatrick's theory to allow for electromagnetically thick walls.

Tokamak vacuum vessels are generally fabricated from a non-ferromagnetic metal such as copper, stainless steel, or Inconel. Up to now, it has been standard practice to avoid (whenever possible) incorporating ferromagnetic materials into tokamaks; first, because the magnetic fields generated by such materials greatly complicate plasma control; and, second, because ferromagnetic materials are known to destabilize ideal external-kink modes [and other magnetohydrodynamical (MHD) instabilities].^{20–22} However, economic and environmental considerations in future tokamak reactors demand that the amount of radioactive waste be kept to an absolute minimum. Hence, it is vitally important that the first wall and blanket, which will play the role of the wall in such devices, be fabricated from a low-activation material. Unfortunately, all of the most promising candidate materials, such as F82H steel,²³ are ferromagnetic. Thus, the final aim of this paper is to assess the impact of wall ferromagnetism on wall-induced tearing mode rotation braking.

This paper is organized as follows. In Sec. II, we determine the response of a ferromagnetic wall, which can be either electromagnetically thin or thick, to the magnetic field generated by a rotating tearing mode. This permits us to write the plasma toroidal angular equation of motion, and, hence, to determine the effect of the wall on the mode rotation frequency. In Sec. III, we examine the limit in which the wall is electromagnetically thin. In Sec. IV, we examine the opposite limit in which the wall is electromagnetically thick. Finally, we summarize our findings in Sec. V.

II. PRELIMINARY ANALYSIS

A. Coordinates

Let us adopt the standard right-handed cylindrical coordinates: r , θ , z . The system is assumed to be periodic in the z -direction with period $2\pi R_0$, where R_0 is the simulated major radius.

B. Plasma equilibrium

The equilibrium magnetic field is written as $\mathbf{B} = (0, B_\theta(r), B_z)$, whereas the equilibrium current density takes the form $\mathbf{J} = (0, 0, J_z(r))$, with $J_z = 0$ for $r > a$. Here, a is the plasma minor radius. Let

$$J(r) = \frac{\mu_0 R_0}{B_z} J_z. \quad (1)$$

It follows that

$$J = \frac{1}{r} \frac{d}{dr} \left(\frac{r^2}{q} \right), \quad (2)$$

where

$$q(r) = \frac{r B_z}{R_0 B_\theta} \quad (3)$$

is the safety-factor profile.

In the following, we shall adopt standard, large aspect-ratio, tokamak orderings, according to which $B_z \gg B_\theta$, $R_0 \gg a$, and $q \sim \mathcal{O}(1)$.¹⁰

C. Perturbed magnetic field

The helical magnetic field associated with a tearing mode is written

$$\delta\mathbf{B} = \epsilon_a B_z a \nabla\psi \times \mathbf{e}_z, \quad (4)$$

where

$$\epsilon_a = \frac{a}{R_0} \ll 1 \quad (5)$$

is the inverse aspect-ratio of the plasma. Let

$$\psi(r, \theta, z, t) = \psi(r, t) e^{i(m\theta - n\phi)}, \quad (6)$$

where

$$\phi = \frac{z}{R_0} \quad (7)$$

is a simulated toroidal angle. Here, ψ is the helical magnetic flux (normalized with respect to $\epsilon_a B_z a$) associated with the tearing mode, $m > 0$ is the poloidal mode number, and $n > 0$ the toroidal mode number. It follows that

$$\delta \mathbf{B} \simeq \epsilon_a B_z a \left(i \frac{m}{r} \psi, -\frac{\partial \psi}{\partial r}, 0 \right). \quad (8)$$

D. Marginally stable ideal-MHD physics

Except in the immediate vicinity of the rational surface, the tearing perturbation within the plasma is governed by the equations of marginally-stable, ideal-MHD, which easily yield the well-known *cylindrical tearing mode equation*:¹⁰

$$\frac{1}{r} \frac{\partial}{\partial r} \left(r \frac{\partial \psi}{\partial r} \right) - \frac{m^2}{r^2} \psi + \frac{J' \psi}{r(1/q_s - 1/q)} = 0. \quad (9)$$

Here, $' \equiv d/dr$, and $q_s = m/n$. We can treat any vacuum regions outside the plasma as zero-inertia plasmas characterized by $J = 0$. In this case, the previous equation simplifies to give

$$\frac{1}{r} \frac{\partial}{\partial r} \left(r \frac{\partial \psi}{\partial r} \right) - \frac{m^2}{r^2} \psi = 0. \quad (10)$$

E. Wall physics

Suppose that the plasma is surrounded by rigid wall of electrical conductivity σ_w , and relative magnetic permeability μ_w , which extends from $r = r_w$ to $r = r_w + \delta_w$, where $r_w \geq a$. Inside the wall, standard electrodynamics reveals that

$$\mu_0 \mu_w \sigma_w \frac{\partial \psi}{\partial r} = \frac{1}{r} \frac{\partial}{\partial r} \left(r \frac{\partial \psi}{\partial r} \right) - \frac{m^2}{r^2} \psi. \quad (11)$$

F. Eigenfunctions and stability parameters

Outside the wall, without loss of generality, we can write

$$\psi(r, t) = \Psi_s(t) \hat{\psi}_s(r) + \Psi_w(t) \hat{\psi}_w(r). \quad (12)$$

Here, $\hat{\psi}_s(r)$ and $\hat{\psi}_w(r)$ are real piecewise continuous functions (which are analytic in the segments $0 < r < r_{s+}$, $r_{s+} < r < r_{w-}$, $r_{w+} < r < \infty$), whereas Ψ_s and Ψ_w are complex parameters. Furthermore,

$$\hat{\psi}_s(r) = \begin{cases} 0 & r \rightarrow 0 \\ 1 & r = r_{s+} \\ 0 & r \geq r_{w-} \end{cases} \quad (13)$$

and

$$\hat{\psi}_w(r) = \begin{cases} 0 & r \leq r_{s+} \\ 1 & r = r_{w-} \\ 0 & r \rightarrow \infty, \end{cases} \quad (14)$$

where $q(r_s) = q_s$. Here, r_s is the minor radius of the rational surface, Ψ_s is the (normalized) reconnected magnetic flux at the rational surface, and Ψ_w is the (normalized) helical magnetic flux that penetrates the wall.

Let

$$E_{ss} = \left[r \frac{d\hat{\psi}_s}{dr} \right]_{r=r_{s-}}^{r=r_{s+}}, \quad (15)$$

$$E_{ww} = -r \frac{d\hat{\psi}_w}{dr} \Big|_{r=r_{w-}} - m, \quad (16)$$

$$E_{sw} = r \frac{d\hat{\psi}_w}{dr} \Big|_{r=r_{s+}}, \quad (17)$$

$$E_{ws} = -r \frac{d\hat{\psi}_s}{dr} \Big|_{r=r_{w-}}. \quad (18)$$

Here, E_{ss} is the conventional ideal-wall tearing stability index (normalized to the plasma minor radius),⁴ E_{ww} is an analogous index that governs the stability of the ideal-plasma resistive wall mode (which is assumed to be stable),²⁴ and E_{sw} and E_{ws} parameterize the electromagnetic coupling between the rational surface and the wall. Now, it follows from Eq. (9) that

$$\frac{d}{dr} \left(\hat{\psi}_w r \frac{d\hat{\psi}_s}{dr} - \hat{\psi}_s r \frac{d\hat{\psi}_w}{dr} \right) = 0, \quad (19)$$

for $r_{s+} \leq r \leq r_{w-}$. Hence, we deduce that

$$r \frac{d\hat{\psi}_s}{dr} \Big|_{r=r_{w-}} = -r \frac{d\hat{\psi}_w}{dr} \Big|_{r=r_{s+}} \quad (20)$$

or

$$E_{ws} = E_{sw}. \quad (21)$$

G. Asymptotic matching

In the vacuum region lying outside the wall, for which $r > r_w + \delta_w$, the appropriate solution of Eq. (10) is

$$\psi(r, t) = \alpha(t) r^{-m}. \quad (22)$$

Hence,

$$r \frac{\partial \psi}{\partial r} \Big|_{r=r_w+\delta_{w+}} = -m \psi \Big|_{r=r_w+\delta_{w+}}. \quad (23)$$

Matching the normal and tangential components of the perturbed magnetic field across $r = r_w + \delta_w$ yields

$$\psi \Big|_{r=r_w+\delta_{w-}} = \psi \Big|_{r=r_w+\delta_{w+}}, \quad (24)$$

$$\mu_w^{-1} r \frac{\partial \psi}{\partial r} \Big|_{r=r_w+\delta_{w-}} = r \frac{\partial \psi}{\partial r} \Big|_{r=r_w+\delta_{w+}}, \quad (25)$$

which implies that the appropriate boundary condition (in the wall material) at the wall's outer radius is

$$r \frac{\partial \psi}{\partial r} \Big|_{r=r_w+\delta_w-} = -\mu_w m \psi \Big|_{r=r_w+\delta_w-}. \quad (26)$$

Equations (12)–(14), (16), (18), and (21) give

$$\psi \Big|_{r=r_w-} = \Psi_w, \quad (27)$$

$$r \frac{\partial \psi}{\partial r} \Big|_{r=r_w-} = -E_{sw} \Psi_s - (E_{ww} + m) \Psi_w. \quad (28)$$

Matching the normal and tangential components of the perturbed magnetic field across $r = r_w$ yields

$$\psi \Big|_{r=r_w-} = \psi \Big|_{r=r_w+}, \quad (29)$$

$$r \frac{\partial \psi}{\partial r} \Big|_{r=r_w-} = \mu_w^{-1} r \frac{\partial \psi}{\partial r} \Big|_{r=r_w+}. \quad (30)$$

Hence, the appropriate boundary condition (in the wall material) at the wall's inner radius is

$$\psi \Big|_{r=r_w+} = \Psi_w. \quad (31)$$

Moreover,

$$\Delta_w \Psi_w = E_{ww} \Psi_w + E_{sw} \Psi_s, \quad (32)$$

where the so-called *wall response function*, Δ_w , is defined

$$\Delta_w = -\mu_w^{-1} \frac{r}{\Psi_w} \frac{\partial \psi}{\partial r} \Big|_{r=r_w+} - m. \quad (33)$$

The wall response function (or, to be more exact, $\Delta \Psi_w \equiv \Delta_w \Psi_w$) parameterizes the helical eddy currents excited in the wall. Equation (32) can be rearranged to give

$$\Psi_w = \frac{E_{sw} \Psi_s}{\Delta_w - E_{ww}}. \quad (34)$$

Finally, asymptotic matching across the rational surface yields

$$\Delta \Psi_s = E_{ss} \Psi_s + E_{sw} \Psi_w. \quad (35)$$

Here, $\Delta \Psi_s$ parameterizes the helical currents flowing in the immediate vicinity of the rational surface.²⁵

H. Electromagnetic braking torque

The net toroidal electromagnetic braking torque acting in the immediate vicinity of the rational surface, as a consequence of eddy currents excited in the wall, is written¹⁰

$$\delta T = \frac{2\pi^2 B_z^2 a^4}{\mu_0 R_0} \delta \hat{T}, \quad (36)$$

where

$$\delta \hat{T} = n \operatorname{Im}(\Delta \Psi_s \Psi_s^*). \quad (37)$$

Thus, it follows from Eqs. (34) and (35) that

$$\delta \hat{T} = -n E_{sw}^2 |\Psi_s|^2 \left[\frac{I_w}{(R_w - E_{ww})^2 + I_w^2} \right], \quad (38)$$

where

$$\Delta_w = R_w + i I_w. \quad (39)$$

Here, R_w and I_w are the real and imaginary parts of the wall response function, respectively.

I. Magnetic island width

The reconnected magnetic flux at the rational surface is associated with an island chain whose full radial width (normalized to the minor radius) is¹⁰

$$W(t) = 4 \left[\frac{|\Psi_s| q_s}{s_s} \right]^{1/2}, \quad (40)$$

where

$$s_s = \frac{r q'}{q} \Big|_{r=r_s} \quad (41)$$

is the magnetic shear at the rational surface.

J. Calculation of wall response function

Inside the wall, let us search for a separable solution of the form

$$\psi(r, t) = \Psi_w(t) \psi_0(r). \quad (42)$$

Substitution of Eq. (42) into Eqs. (11), (26), and (31) yields

$$\gamma \mu_0 \mu_w \sigma_w \psi_0 = \frac{1}{r} \frac{d}{dr} \left(r \frac{d\psi_0}{dr} \right) - \frac{m^2}{r^2} \psi_0, \quad (43)$$

$$\psi_0 \Big|_{r=r_w+} = 1, \quad (44)$$

$$r \frac{d\psi_0}{dr} \Big|_{r=r_w+\delta_w-} = -\mu_w m \psi_0 \Big|_{r=r_w+\delta_w-}, \quad (45)$$

where

$$\gamma = \frac{d \ln \Psi_w}{dt}. \quad (46)$$

Finally, Eq. (33) gives

$$\Delta_w = -\mu_w^{-1} r \frac{d\psi_0}{dr} \Big|_{r=r_w-} - m. \quad (47)$$

According to Eq. (43),

$$\psi_0(r) \equiv \psi_0(z) = A K_m(z) + B I_m(z), \quad (48)$$

where $z = pr$, $p = (\gamma \mu_0 \mu_w \sigma_w)^{1/2}$, A and B are arbitrary constants, and I_m and K_m are modified Bessel functions. It follows from Eq. (45) that

$$\frac{A}{B} = \frac{z_2 I_{m-1}(z_2) + k I_m(z_2)}{z_2 K_{m-1}(z_2) - k K_m(z_2)}, \quad (49)$$

where $z_2 = p(r_w + \delta_w)$, and

$$k = m(\mu_w - 1). \quad (50)$$

Hence, Eq. (44) gives

$$\psi_0(z) = \frac{Q(z, z_2)}{Q(z_1, z_2)} \quad (51)$$

and

$$\frac{d\psi_0}{d \ln z} = \frac{d\psi_0}{d \ln r} = - \left[\frac{z P(z, z_2) + m Q(z, z_2)}{Q(z_1, z_2)} \right], \quad (52)$$

where $z_1 = p r_w$, and

$$P(z, z_2) = z_2 [I_{m-1}(z_2) K_{m-1}(z) - I_{m-1}(z) K_{m-1}(z_2)] + k [I_m(z_2) K_{m-1}(z) + I_{m-1}(z) K_m(z_2)], \quad (53)$$

$$Q(z, z_2) = z_2 [I_{m-1}(z_2) K_m(z) + I_m(z) K_{m-1}(z_2)] + k [I_m(z_2) K_m(z) - I_m(z) K_m(z_2)]. \quad (54)$$

Note that $z_2 P(z_2, z_2) = k Q(z_2, z_2)$, in accordance with Eq. (45). It follows from Eqs. (47) and (52) that

$$\Delta_w = \frac{z_1 P(z_1, z_2)}{\mu_w Q(z_1, z_2)} - \frac{k}{\mu_w}. \quad (55)$$

Let

$$\tau_d = \mu_0 \mu_w \sigma_w \delta_w^2, \quad (56)$$

$$\epsilon_w = \frac{\delta_w}{r_w}, \quad (57)$$

so that $z_1 = (\gamma \tau_d)^{1/2} / \epsilon_w$ and $z_2 = z_1 (1 + \epsilon_w)$. Here, τ_d is the wall diffusion time (i.e., the time required for magnetic flux to diffuse from the wall's inner to its outer radius), whereas ϵ_w parameterizes the wall thickness. Now, in the limit $|z| \gg 1$,

$$I_m(z) \simeq \frac{e^z}{\sqrt{2\pi z}}, \quad (58)$$

$$K_m(z) \simeq \frac{e^{-z}}{\sqrt{(2/\pi)z}}. \quad (59)$$

Hence, in the limit $|z_1| \gg 1$, or

$$\gamma \tau_d \gg \epsilon_w^2, \quad (60)$$

we obtain

$$P(z, z_2) \simeq \frac{1}{\hat{\gamma}^{1/2}} [\hat{\gamma}^{1/2} \sinh(\hat{\gamma}^{1/2} s) + k \epsilon_w \cosh(\hat{\gamma}^{1/2} s)], \quad (61)$$

$$Q(z, z_2) \simeq \frac{1}{\hat{\gamma}^{1/2}} [\hat{\gamma}^{1/2} \cosh(\hat{\gamma}^{1/2} s) + k \epsilon_w \sinh(\hat{\gamma}^{1/2} s)], \quad (62)$$

where $\hat{\gamma} = \gamma \tau_d$, $s = (r_w + \delta_w - r) / \delta_w = (z_2 - z) / \hat{\gamma}^{1/2}$, and it is assumed that

$$0 < \epsilon_w \ll 1. \quad (63)$$

It follows from Eq. (55) that

$$\Delta_w \simeq \frac{1}{\mu_w \epsilon_w} \left(\hat{\gamma}^{1/2} \left[\frac{\hat{\gamma}^{1/2} \tanh(\hat{\gamma}^{1/2}) + k \epsilon_w}{\hat{\gamma}^{1/2} + k \epsilon_w \tanh(\hat{\gamma}^{1/2})} \right] - k \epsilon_w \right). \quad (64)$$

Note that there is a small inconsistency in the analysis presented in this section. Equation (42) asserts that ψ_0 is not a function of t , whereas it is clear from Eq. (51) that $\psi_0 \equiv \psi_0(z)$ does depend on t , because z depends on γ , and γ is time-dependent in a non-steady-state situation. It is easily demonstrated that our expression for the wall response function is not invalidated by this inconsistency as long as

$$\left| \frac{\partial \ln \psi_0}{\partial t} \right|_{z=z_1} \ll |\gamma|, \quad (65)$$

which reduces to

$$\left| \mu_w (\Delta_w + m) \frac{d \ln \gamma}{dt} \right| \ll |\gamma|. \quad (66)$$

If the previous inequality is not satisfied then transient wall solutions have to be incorporated into the analysis, as described in Refs. 15 and 26.

K. Plasma equation of toroidal angular motion

Let

$$\Omega_\phi(r, t) = \Omega_\phi^{(0)}(r) + \Delta\Omega_\phi(r, t) \quad (67)$$

be the plasma toroidal angular velocity profile. Here, $\Omega_\phi^{(0)}(r)$ is the steady-state profile in the absence of the braking torque ultimately induced by the helical eddy currents excited in the wall, whereas $\Delta\Omega_\phi(r, t)$ is the modification to the rotation profile generated by these currents. The plasma equation of toroidal angular motion is written as¹⁰

$$\rho r \frac{\partial \Delta\Omega_\phi}{\partial t} - \mu \frac{\partial}{\partial r} \left(r \frac{\partial \Delta\Omega_\phi}{\partial r} \right) = \frac{\delta T}{4\pi^2 R_0^3} \delta(r - r_s), \quad (68)$$

where ρ and μ are the plasma mass density and perpendicular viscosity, respectively. For the sake of simplicity, these quantities are assumed to be uniform across the plasma. Finally, the boundary conditions satisfied by the perturbed toroidal angular velocity profile are¹⁰

$$\frac{\partial \Delta\Omega_\phi(0, t)}{\partial r} = \Delta\Omega_\phi(a, t) = 0. \quad (69)$$

L. No-slip constraint

The conventional *no-slip constraint* demands that the island chain co-rotate with the plasma at the rational surface.¹⁰ (This constraint holds as long as the island width is

much greater than the linear layer width at the rational surface.) In other words,

$$\Psi_s(t) = |\Psi_s|(t) \exp \left[-i \int_0^t \omega(t') dt' \right], \quad (70)$$

where

$$\omega(t) = \omega_0 - n \Delta \Omega_\phi(r_s, t). \quad (71)$$

Here,

$$\omega_0 = -n \Omega_\phi^{(0)}(r_s) \quad (72)$$

is the steady-state island rotation frequency in the absence of the braking torque. Incidentally, we are assuming that the plasma poloidal angular velocity profile is fixed, as a consequence of strong poloidal flow damping.¹⁰

M. Normalized plasma equation of toroidal angular motion

Let $\hat{r} = r/a$, $\hat{r}_s = r_s/a$, $\Omega(\hat{r}, t) = n \Delta \Omega_\phi / \omega_0$, $\tau_H = (R_0 / n s_s) (\mu_0 \rho / B_z^2)^{1/2}$, and $\tau_M = \rho a^2 / \mu$. Here, τ_H and τ_M are the conventional *hydromagnetic* and *momentum confinement* timescales, respectively.¹⁰ Equations (36), (38), (40), (68), and (71) yield the normalized no-slip constraint

$$\omega(t) = \omega_0 [1 - \Omega(\hat{r}_s, t)], \quad (73)$$

as well as the normalized plasma equation of toroidal angular motion

$$\tau_M \frac{\partial \Omega}{\partial t} - \frac{1}{\hat{r}} \frac{\partial}{\partial \hat{r}} \left(\hat{r} \frac{\partial \Omega}{\partial \hat{r}} \right) = -T \frac{\delta(\hat{r} - \hat{r}_s)}{\hat{r}}, \quad (74)$$

where

$$T(t) = \hat{W}^4 \left[\frac{I_w}{(R_w - E_{ww})^2 + I_w^2} \right]. \quad (75)$$

Here,

$$\hat{W}(t) = \frac{W}{W_0} \quad (76)$$

and

$$W_0 = 4 \left[\frac{2 \omega_0 \tau_H^2}{E_{sw}^2 \tau_M} \left(\frac{q_s}{\epsilon_a} \right)^2 \right]^{1/4}. \quad (77)$$

Finally, it follows from Eq. (69) that

$$\frac{\partial \Omega(0, t)}{\partial \hat{r}} = \Omega(1, t) = 0. \quad (78)$$

Note that $R_w = R_w(\gamma)$ and $I_w = I_w(\gamma)$, where

$$\gamma = -i \omega + 2 \frac{d \ln \hat{W}}{dt} - \frac{d \ln (R_w - E_{ww} + i I_w)}{dt}. \quad (79)$$

Here, use has been made of Eqs. (34), (39), (40), (46), (70), and (76).

N. Solution of normalized plasma equation of toroidal angular motion

Let

$$u_k(\hat{r}) = \frac{\sqrt{2} J_0(j_{0,k} \hat{r})}{J_1(j_{0,k})}, \quad (80)$$

where $j_{0,k}$ denotes the k th zero of the J_0 Bessel function. It is easily demonstrated that

$$\int_0^1 \hat{r} u_k(\hat{r}) u_{k'}(\hat{r}) d\hat{r} = \delta_{kk'} \quad (81)$$

and

$$\delta(\hat{r} - \hat{r}_s) = \sum_{k=1, \infty} \hat{r} u_k(\hat{r}_s) u_k(\hat{r}). \quad (82)$$

Let us write

$$\Omega(\hat{r}, t) = \sum_{k=1, \infty} h_k(t) \frac{u_k(\hat{r})}{u_k(\hat{r}_s)}, \quad (83)$$

which automatically satisfies the boundary conditions (78). Substitution into Eq. (74) yields¹⁵

$$\tau_M \frac{dh_k}{dt} + j_{0,k}^2 h_k = -T(t) [u_k(\hat{r}_s)]^2, \quad (84)$$

where use has been made of Eqs. (80)–(82). Finally, Eqs. (73) and (83) give

$$\omega(t) = \omega_0 \left(1 - \sum_{k=1, \infty} h_k \right). \quad (85)$$

O. Rutherford island width evolution equation

The saturated width of the island chain is determined by the Rutherford island width evolution equation, which takes the form^{5,10}

$$\tau_R \frac{d}{dt} \left(\frac{W}{r_s} \right) = \text{Re} \left(\frac{\Delta \Psi_s}{\Psi_s} \right), \quad (86)$$

where $\tau_R = 0.8227 \mu_0 r_s^2 / \eta$, and η is the plasma resistivity. It follows from Eqs. (34), (35), and (39) that

$$\tau_R \frac{d}{dt} \left(\frac{W}{r_s} \right) = E_{ss}(W) + \frac{E_{sw}^2 [R_w(\omega) - E_{ww}]}{[R_w(\omega) - E_{ww}]^2 + [I_w(\omega)]^2}. \quad (87)$$

Here, we have explicitly taken account of the fact that E_{ss} (the conventional tearing Δ' parameter) is generally a (fairly complicated) function of the island width,^{6–8} whereas (in a steady state) the real and imaginary parts of the wall response function, R_w and I_w , respectively, are functions of the island frequency, ω . In the following, for the sake of simplicity, we shall neglect any dependence of the saturated

island width on the island frequency. This is equivalent to neglecting the second term on the right-hand side of the previous equation with respect to the first. Thus, the saturated island width is determined by the solution of

$$0 = E_{ss}(W). \quad (88)$$

Note that it would be a fairly straightforward (but tedious) task to incorporate the frequency dependence of the island width into the following analysis.

III. THIN-WALL REGIME

A. Governing equations

Consider the *thin-wall regime*, which is characterized by $|\gamma \tau_d| \ll 1$. In this regime, the wall is “electromagnetically thin”: i.e., its radial thickness is much less than the skin depth in the wall material (calculated with the growth-rate γ). It follows from Eq. (64) that the wall response function reduces to

$$\Delta_w = \frac{\gamma \tau_w}{1 + k \epsilon_w} - m \left(\frac{k \epsilon_w}{1 + k \epsilon_w} \right) \quad (89)$$

in the thin-wall regime, where

$$\tau_w = \mu_0 \sigma_w \delta_w r_w \quad (90)$$

is the *wall time-constant* (i.e., the effective L/R time of the wall). Here, for the sake of simplicity, it is assumed that $k \simeq m \mu_w \gg 1$. The approximations used in deriving Eq. (89) are valid provided

$$\epsilon_w^2 \left(\frac{m}{k \epsilon_w} \right) \ll |\gamma \tau_w| \ll \frac{m}{k \epsilon_w}. \quad (91)$$

Let us suppose that the first term on the right-hand side of Eq. (79) is dominant. It follows that

$$\gamma = -i \omega, \quad (92)$$

which implies that [see Eq. (39)]

$$R_w = -m \left(\frac{k \epsilon_w}{1 + k \epsilon_w} \right), \quad (93)$$

$$I_w = -\frac{\omega \tau_w}{1 + k \epsilon_w}. \quad (94)$$

Thus, the approximations employed in writing Eq. (92) are valid provided

$$\left| \frac{1}{\omega} \frac{d \ln W}{dt} \right|, \left| \frac{1}{\omega} \frac{d \ln \omega}{dt} \right| \ll 1. \quad (95)$$

B. Thin-wall rotation-braking equations

Let

$$\hat{t} = \frac{t}{\tau_M}, \quad \hat{\omega} = \frac{\omega}{\omega_0}, \quad \kappa = \left(\frac{m}{\omega_0 \tau_w} \right) \left[\frac{2 + (1 + \zeta) k \epsilon_w}{1 - \zeta} \right],$$

$$\zeta = \left(\frac{r_s}{r_w} \right)^{2m}, \quad X = \left(\frac{W}{W_1} \right)^4,$$

$$W_1 = \left[\frac{\omega_0 \tau_w}{4 \ln(1/\hat{r}_s) (1 + k \epsilon_w)} \right]^{1/4} W_0. \quad (96)$$

Equations (75), (84), (85), (93), (94), and (96) yield the *thin-wall rotation-braking equations*:

$$\frac{dh_k}{d\hat{t}} + j_{0,k}^2 h_k = \frac{X}{4 \ln(1/\hat{r}_s)} \left(\frac{\hat{\omega}}{\kappa^2 + \hat{\omega}^2} \right) [u_k(\hat{r}_s)]^2, \quad (97)$$

$$\hat{\omega} = 1 - \sum_{k=1, \infty} h_k. \quad (98)$$

Here, for the sake of simplicity, E_{ww} has been given the conventional value

$$E_{ww} = -\frac{2m}{1 - \zeta}, \quad (99)$$

which corresponds to the absence of plasma current in the region $r > r_{s+}$. In Eqs. (97) and (98), \hat{t} is the normalized time, $\hat{\omega}$ is the normalized island rotation frequency, \hat{r}_s is the normalized minor radius of the rational surface, κ (primarily) parameterizes the intrinsic plasma rotation, and X parameterizes the island width.

C. Steady-state solutions

In a steady-state (i.e., $d/d\hat{t} = 0$), Eq. (97) yields

$$h_k = \frac{X}{4 \ln(1/\hat{r}_s)} \left(\frac{\hat{\omega}}{\kappa^2 + \hat{\omega}^2} \right) \frac{[u_k(\hat{r}_s)]^2}{j_{0,k}^2}, \quad (100)$$

which can be combined with Eq. (98) to give the *thin-wall torque-balance equation*:¹⁰

$$1 - \hat{\omega} = \frac{X}{4} \left(\frac{\hat{\omega}}{\kappa^2 + \hat{\omega}^2} \right). \quad (101)$$

Here, use has been made of the identity

$$\sum_{k=1, \infty} \frac{[u_k(\hat{r}_s)]^2}{j_{0,k}^2} \equiv \ln \left(\frac{1}{\hat{r}_s} \right). \quad (102)$$

The right-hand side of Eq. (101) represents the electromagnetic braking torque, due to eddy currents induced in the wall, which acts to reduce the island rotation frequency, whereas the left-hand side represents the viscous restoring torque that acts to maintain the rotation.

Equation (101) yields

$$\frac{dX}{d\hat{\omega}} = -\frac{4(\kappa^2 - \hat{\omega}^2 + 2\hat{\omega}^3)}{\hat{\omega}^2}, \quad (103)$$

$$\frac{d^2X}{d\hat{\omega}^2} = -\frac{8(-\kappa^2 + \hat{\omega}^3)}{\hat{\omega}^3}. \quad (104)$$

In Refs. 10, 27, and 28, it is argued that solutions of Eq. (101) for which $dX/d\hat{\omega} < 0$ (i.e., solutions for which the island rotation frequency decreases as the island width increases) are dynamically stable, whereas solutions for which the $dX/d\hat{\omega} > 0$ are dynamically unstable. This argument leads to the conclusion that, when $\kappa < \kappa_c = 1/\sqrt{27}$ (i.e., when the intrinsic plasma rotation is sufficiently high), the general solution of the torque-balance equation exhibits a “forbidden band” of island rotation frequencies. [Incidentally, the value of κ_c is obtained from the simultaneous solution of $dX/d\hat{\omega} = d^2X/d\hat{\omega}^2 = 0$, with $dX/d\hat{\omega}$ and $d^2X/d\hat{\omega}^2 = 0$ specified by Eqs. (103) and (104), respectively. At the critical point, $\hat{\omega} = \hat{\omega}_c = 1/3$ and $X = X_c = 32/27$.] This band separates a branch of dynamically stable low-frequency solutions from a branch of dynamically stable high-frequency solutions. Thus, when a low-frequency solution crosses the lower boundary of the forbidden band, it becomes dynamically unstable, and there is (presumably) a bifurcation to a high-frequency solution (characterized by the same values of X and κ). Likewise, when a high-frequency solution crosses the upper boundary of the forbidden band, it becomes dynamically unstable, and there is (presumably) a bifurcation to a low-frequency solution.

The critical values of X and $\hat{\omega}$ where the aforementioned bifurcations take place, which are numerically determined from the solution of $dX/d\hat{\omega} = 0$, with $dX/d\hat{\omega}$ specified by Eq. (103), are shown in Figs. 1 and 2. It can be seen that, to a good approximation, there is a bifurcation from a high-frequency solution [i.e., $\hat{\omega} \sim \mathcal{O}(1)$] to a low-frequency solution [i.e., $\hat{\omega} \sim \mathcal{O}(\kappa)$] when X exceeds the critical value

$$X_+ \simeq 1 + 5\kappa^2. \quad (105)$$

Just before the bifurcation, $\hat{\omega}$ takes the value

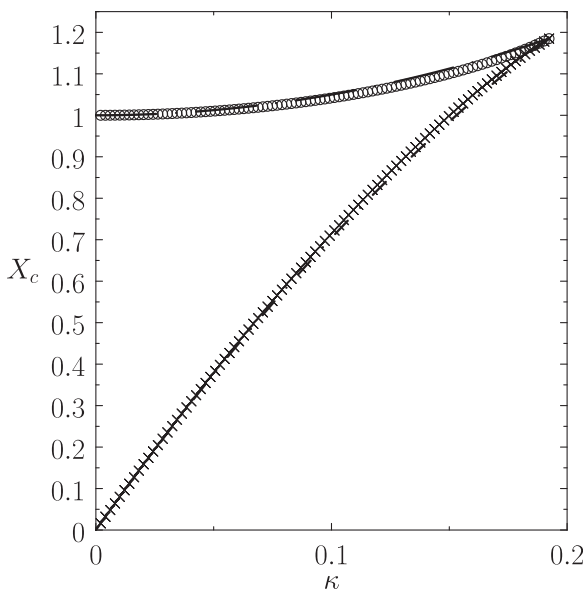


FIG. 1. Bifurcation thresholds derived from the thin-wall torque-balance equation. The circles show the critical X value above which high-frequency solutions bifurcate to low-frequency solutions, plotted as a function of κ . Similarly, the crosses show the critical X value below which low-frequency solutions bifurcate to high-frequency solutions. The long-dashed-dotted curve shows the analytic approximation $X = 1 + 5\kappa^2$. The short-dashed-dotted curve shows the analytic approximation $X = 8\kappa - (8\sqrt{27} - 32)\kappa^2$.

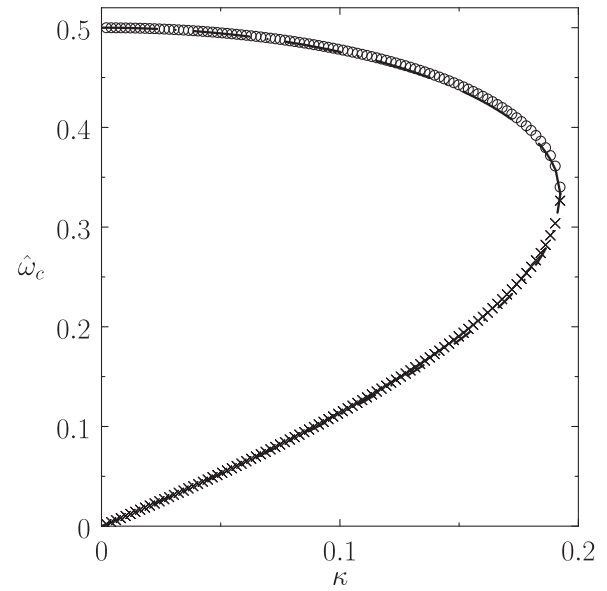


FIG. 2. Bifurcation thresholds derived from the thin-wall torque-balance equation. The circles show the critical $\hat{\omega}$ value at which high-frequency solutions bifurcate to low-frequency solutions, plotted as a function of κ . Similarly, the crosses show the critical $\hat{\omega}$ value at which low-frequency solutions bifurcate to high-frequency solutions. The long-dashed-dotted curve shows the analytic approximation $\hat{\omega} = (1/3) + (1/6)\sqrt{1 - 27\kappa^2}$. The short-dashed-dotted curve shows the analytic approximation $\hat{\omega} = (1/3) - (1/3)\sqrt{1 - 6\kappa - 9(3 - 2\sqrt{3})\kappa^2}$.

$$\hat{\omega}_+ \simeq \frac{1}{3} + \frac{1}{6}\sqrt{1 - 27\kappa^2}. \quad (106)$$

On the other hand, there is a bifurcation from a low-frequency to a high-frequency solution when X falls below the critical value

$$X_- \simeq 8\kappa - (8\sqrt{27} - 32)\kappa^2. \quad (107)$$

Just before the bifurcation, $\hat{\omega}$ takes the value

$$\hat{\omega}_- \simeq \frac{1}{3} - \frac{1}{3}\sqrt{1 - 6\kappa - 9(3 - 2\sqrt{3})\kappa^2}. \quad (108)$$

Of course, Eqs. (105)–(108) are only valid when $\kappa < \kappa_c$. For $\kappa \geq \kappa_c$, there are no bifurcations, which implies that $\hat{\omega}$ varies smoothly and reversibly with X . The fact that $X_- < X_+$ suggests that the high-frequency/low-frequency bifurcation cycle exhibits considerable hysteresis.¹⁰ Note, incidentally, that Eqs. (105)–(108) are analytic approximations to the exact solutions (which cannot be expressed in closed forms).

D. Time-dependent solutions

Figure 3 shows a typical solution of the thin-wall rotation-braking equations, (97)–(98), in which the island width parameter, X , is very slowly (compared to the momentum confinement timescale) ramped up from zero to some maximum value that exceeds that at which the bifurcation from high-frequency to low-frequency solution branches is predicted to occur (according to torque-balance theory), and then very slowly ramped back down to zero. It can be seen

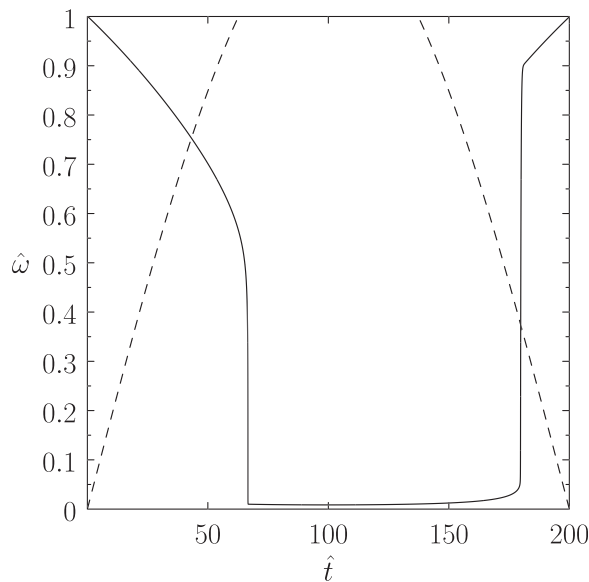


FIG. 3. Solution of the thin-wall rotation-braking equations, calculated with $\kappa = 0.05$, $\hat{r}_s = 0.5$, and $X = 1.2 \sin(\pi \hat{t}/200)$. The solid curve shows the normalized island rotation frequency, $\hat{\omega}$, plotted as a function of the normalized time. The dashed curve shows the imposed time variation of the island width parameter, X .

that, at first, the normalized plasma rotation frequency, $\hat{\omega}$, decreases smoothly as X increases. Eventually, however, when the rotation frequency has been reduced to about half of its original value ($\hat{\omega} = 1$), the frequency drops precipitously to a very low value (compared to its original value). This is the high-frequency to low-frequency bifurcation. Conversely, the rotation frequency initially rises smoothly, as X decreases, although it still takes a comparatively low value. Eventually, however, the frequency rises precipitously, attaining a value that is comparable with its original one. This is the low-frequency to high-frequency bifurcation. Incidentally, the hysteresis in the high-frequency/low-frequency bifurcation cycle is illustrated by the strong asymmetry (about $\hat{t} = 100$) evident in the $\hat{\omega}$ - \hat{t} curve plotted in Fig. 3.

Let $\Gamma = |d\hat{\omega}/d\hat{t}|$ be the normalized acceleration/deceleration in the island rotation frequency. In the following, the start and end times of the high-to-low-frequency bifurcation are conveniently defined as the times at which Γ first exceeds the critical value 0.05, and subsequently first falls below this value, respectively. (Note that, except during the bifurcations, Γ is typically much smaller than 0.05.) The start and end times of the low-to-high-frequency bifurcation are defined in an analogous manner.

Figures 4 and 5 show the bifurcation thresholds (i.e., the values of X and $\hat{\omega}$ at the start times of the high-to-low-frequency and low-to-high-frequency bifurcations) determined from the thin-wall rotation-braking equations, as a function of the parameter κ . In all cases, $X(t)$ is ramped up and down again, in the manner described in the caption to Fig. 3. Also, shown are the analytic approximations (105)–(108) that were previously derived from torque-balance theory. It is clear that the analytic approximations are fairly accurate, which confirms, first, that torque-balance theory is capable of correctly predicting the occurrence of the high-to-low-frequency

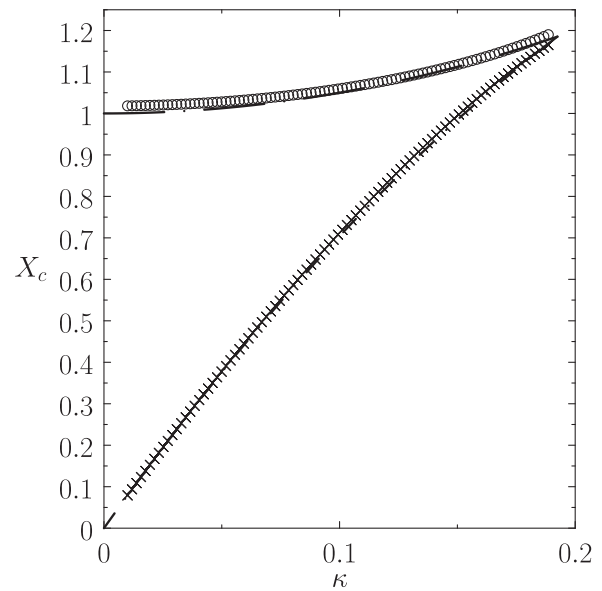


FIG. 4. Bifurcation thresholds derived from the thin-wall rotation-braking equations, with $\hat{r}_s = 0.5$. The circles show the critical X value above which high-frequency solutions bifurcate to low-frequency solutions, plotted as a function of κ . Similarly, the crosses show the critical X value below which low-frequency solutions bifurcate to high-frequency solutions. The long-dashed-dotted curve shows the analytic approximation $X = 1 + 5\kappa^2$. The short-dashed-dotted curve shows the analytic approximation $X = 8\kappa - (8\sqrt{27} - 32)\kappa^2$.

and low-to-high-frequency bifurcations, and, second, that solutions of the thin-wall torque-balance equation characterized by $dX/d\hat{\omega} > 0$ are indeed dynamically unstable.

Of course, torque-balance theory is incapable of predicting the duration of a given bifurcation. Figure 6 shows the durations (i.e., the difference between the end and start

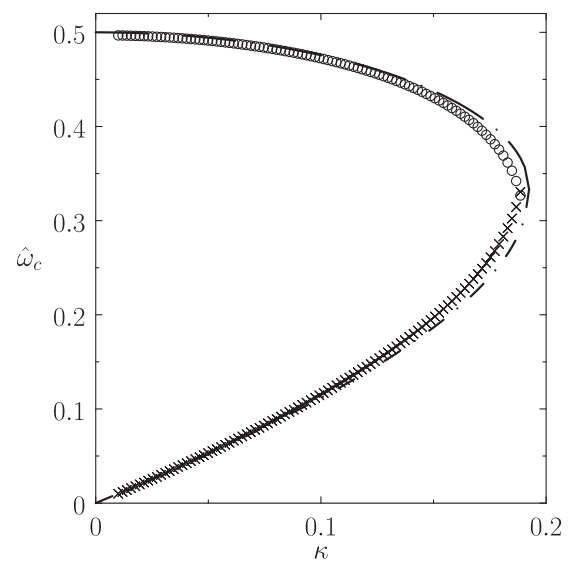


FIG. 5. Bifurcation thresholds derived from the thin-wall rotation-braking equations, with $\hat{r}_s = 0.5$. The circles show the critical $\hat{\omega}$ value at which high-frequency solutions bifurcate to low-frequency solutions, plotted as a function of κ . Similarly, the crosses show the critical $\hat{\omega}$ value at which low-frequency solutions bifurcate to high-frequency solutions. The long-dashed-dotted curve shows the analytic approximation $\hat{\omega} = (1/3) + (1/6)\sqrt{1 - 27\kappa^2}$. The short-dashed-dotted curve shows the analytic approximation $\hat{\omega} = (1/3) - (1/3)\sqrt{1 - 6\kappa - 9(3 - 2\sqrt{3})\kappa^2}$.

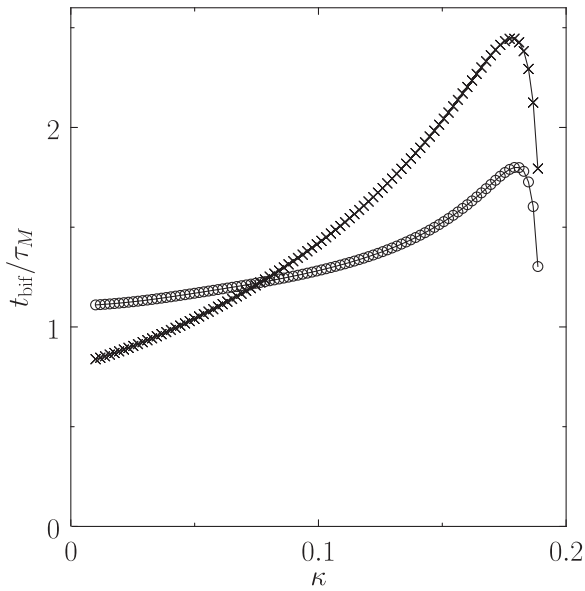


FIG. 6. Bifurcations times derived from the thin-wall rotation-braking equations, with $\hat{r}_s = 0.5$. The circles show the time required for the high-frequency to low-frequency bifurcation, plotted as a function of κ . The crosses show the time required for the low-frequency to high-frequency bifurcation.

times, as defined previously) of the high-to-low-frequency and low-to-high-frequency bifurcations determined from the thin-wall rotation-braking equations, as a function of the parameter κ . As before, $X(t)$ is ramped up and down again, in the manner described in the caption to Fig. 3. It is clear that, in order to reach completion, both types of bifurcations require a time interval whose duration is of order a momentum confinement time. Moreover, at small κ , the low-to-high-frequency bifurcation is slightly faster than the high-to-low-frequency bifurcation, whereas the opposite is true at high κ .

It is apparent, from the preceding discussion, that [see Eq. (92)]

$$\left| \frac{d \ln \gamma}{dt} \right| \simeq \left| \frac{d \ln \omega}{dt} \right| \lesssim \frac{1}{\tau_M}. \quad (109)$$

Hence, the inequalities (95) yield

$$\omega_0 \tau_M, \omega_0 \tau_W \gg 1, \quad (110)$$

where τ_W is the timescale on which the island width varies. Furthermore, the inequality (66) reduces to (assuming that $k \epsilon_w \ll 1$ —see Sec. III E)

$$\tau_M \gg \mu_w \tau_w. \quad (111)$$

Finally, according to Eq. (91), the thin-wall regime only holds when (using $k \simeq m \mu_w$)

$$\frac{\epsilon_w}{\mu_w} \ll \omega_0 \tau_w \ll \frac{1}{\mu_w \epsilon_w}. \quad (112)$$

Thus, the previous three inequalities are the criteria for the validity of the theory presented in this section.

E. Effect of wall ferromagnetism

It follows from Eqs. (50), (57), (77), (96), (105), and (107) that, in the thin-wall regime, the critical island width above which the high-to-low-frequency bifurcation is triggered can be written as

$$W_+ \simeq \left\{ \left[\frac{2 + (1 + \zeta) \lambda_c}{1 + \lambda} \right] \left(27 + 5 \left[\frac{2 + (1 + \zeta) \lambda}{2 + (1 + \zeta) \lambda_c} \right]^2 \right) \right\}^{1/4} W_2, \quad (113)$$

where

$$W_2 = \left[\frac{2^5}{\sqrt{27}} \frac{\omega_0 \tau_H^2}{\tau_M} \frac{(q_s / \epsilon_a)^2}{m \ln(a / r_s)} \left(\frac{1}{\zeta} - 1 \right) \right]^{1/4}, \quad (114)$$

$$\lambda \equiv k \epsilon_w = m (\mu_w - 1) \frac{\delta_w}{r_w}, \quad (115)$$

$$\lambda_c = \left(\frac{\omega_0 \tau_w}{\sqrt{27} m} \right) \left(\frac{1 - \zeta}{1 + \zeta} \right) - \frac{2}{1 + \zeta}. \quad (116)$$

Likewise, the critical island width below which the low-to-high-frequency bifurcation is triggered takes the form

$$W_- \simeq \left\{ \left[\frac{2 + (1 + \zeta) \lambda}{1 + \lambda} \right] \times \left(8\sqrt{27} - (8\sqrt{27} - 32) \left[\frac{2 + (1 + \zeta) \lambda}{2 + (1 + \zeta) \lambda_c} \right] \right) \right\}^{1/4} W_2. \quad (117)$$

Incidentally, assuming, for the sake of simplicity, that there is negligible plasma current in the region $r > r_{s+}$, it is easily demonstrated that

$$E_{sw} = 2m \left(\frac{\zeta^{1/2}}{1 - \zeta} \right), \quad (118)$$

where $\zeta = (r_s / r_w)^{2m}$. This result has been incorporated into Eq. (114).

There are bifurcations between high-frequency and low-frequency solution branches when λ , which parameterizes the degree of wall ferromagnetism, lies in the range $0 < \lambda < \lambda_c$. For $\lambda \geq \lambda_c$, there are no bifurcations, and the island frequency consequently varies smoothly and reversibly as the island width varies. If $\lambda_c < 0$ then there are no bifurcations, irrespective of the value of λ . According to Eq. (91), the thin-wall ordering is only valid provided

$$\lambda \ll \frac{1 - \zeta}{\sqrt{27} [2 + (1 + \zeta) \lambda_c]}. \quad (119)$$

Thus, in order to have bifurcations in the thin-wall regime, we require

$$0 < \lambda_c [2 + (1 + \zeta) \lambda_c] \ll \frac{1 - \zeta}{\sqrt{27}}. \quad (120)$$

However, it is clear that if $0 < \lambda < \lambda_c$, and the previous inequality is satisfied, then $0 < \lambda \ll 1$. In this case, it follows from Eqs. (113) and (117) that the bifurcation thresholds only exhibit a very weak dependence on λ . In other words, in the thin-wall regime, wall ferromagnetism has little effect on the bifurcation thresholds. In fact, the main effect of increasing ferromagnetism (i.e., increasing λ) is to cause the inequality (119) to be violated, and, hence, to push the system into the thick-wall regime described in Sec. IV.

Incidentally, in the previous expressions, ω_0 is the island rotation frequency in the absence of wall braking, τ_H and τ_M are the hydromagnetic and momentum confinement time-scales, respectively (see Sec. II M), τ_w is the wall time-constant [see Eq. (90)], r_w is the wall minor radius, δ_w is the wall radial thickness, μ_w is the wall relative permeability, m is the poloidal mode number of the tearing mode, q_s is the safety-factor at the associated rational surface, r_s is the minor radius of the rational surface, and a is the plasma minor radius.

IV. THICK-WALL REGIME

A. Governing equations

Consider the *thick-wall regime*, which is characterized by $|\gamma \tau_d| \gg 1$. In this regime, the wall is “electromagnetically thick”: i.e., its radial thickness is much greater than the skin depth in the wall material (calculated with the growth-rate γ). It follows from Eq. (64) that the wall response function reduces to

$$\Delta_w = \left(\frac{\gamma \tau_w m}{k \epsilon_w} \right)^{1/2} - m \quad (121)$$

in the thick-wall regime. Here, it is again assumed that $k \simeq m \mu_w \gg 1$. The approximations used in deriving Eq. (121) are valid provided

$$\frac{m}{k \epsilon_w} \ll |\gamma \tau_w|. \quad (122)$$

Let us suppose that the first term on the right-hand side of Eq. (79) is dominant. It follows that

$$\gamma = -i \omega, \quad (123)$$

which implies that

$$R_w = \left(\frac{\omega \tau_w m}{2k \epsilon_w} \right)^{1/2} - m, \quad (124)$$

$$I_w = - \left(\frac{\omega \tau_w m}{2k \epsilon_w} \right)^{1/2}. \quad (125)$$

Thus, the approximations employed in writing Eq. (123) are valid provided

$$\left| \frac{1}{\omega} \frac{d \ln W}{dt} \right|, \quad \left| \frac{1}{\omega} \frac{d \ln \omega}{dt} \right| \ll 1. \quad (126)$$

B. Thick-wall rotation-braking equations

Let

$$\kappa' = \left(\frac{m k \epsilon_w}{\omega_0 \tau_w} \right) \left(\frac{1 + \zeta}{1 - \zeta} \right)^2, \quad X' = \left(\frac{W}{W_1'} \right)^4, \\ W_1' = \left(\frac{8 \omega_0 \tau_w m}{27 [\ln(1/\hat{r}_s)]^2 k \epsilon_w} \right)^{1/8} W_0. \quad (127)$$

Equations (75), (84), (85), (124), (125), and (127) yield the *thick-wall rotation-braking equations*

$$\frac{d h_k}{d \hat{t}} + j_{0,k}^2 h_k = \frac{X'}{\sqrt{27/4} \ln(1/\hat{r}_s)} \left(\frac{\hat{\omega}^{1/2}}{\kappa' + \sqrt{2 \kappa' \hat{\omega} + \hat{\omega}}} \right) [u_k(\hat{r}_s)]^2, \quad (128)$$

$$\hat{\omega} = 1 - \sum_{k=1, \infty} h_k. \quad (129)$$

Here, E_{ww} has again been given the conventional value specified in Eq. (99). As before, \hat{t} is the normalized time, $\hat{\omega}$ is the normalized island rotation frequency, \hat{r}_s is the normalized minor radius of the rational surface, κ' parameterizes the intrinsic plasma rotation, and X' parameterizes the island width.

C. Steady-state solutions

In a steady-state (i.e., $d/d\hat{t} = 0$), Eq. (128) yields

$$h_k = \frac{X'}{\sqrt{27/4} \ln(1/\hat{r}_s)} \left(\frac{\hat{\omega}^{1/2}}{\kappa' + \sqrt{2 \kappa' \hat{\omega} + \hat{\omega}}} \right) \frac{[u_k(\hat{r}_s)]^2}{j_{0,k}^2}, \quad (130)$$

which can be combined with Eq. (129) to give the *thick-wall torque-balance equation*

$$1 - \hat{\omega} = \frac{X'}{\sqrt{27/4}} \left(\frac{\hat{\omega}^{1/2}}{\kappa' + \sqrt{2 \kappa' \hat{\omega} + \hat{\omega}}} \right). \quad (131)$$

Here, use has been made of the identity (102). As before, the right-hand side of Eq. (131) represents the electromagnetic braking torque, due to eddy currents induced in the wall, which acts to reduce the island rotation frequency, whereas the left-hand side represents the viscous restoring torque that acts to maintain the rotation.

Equation (101) yields

$$\frac{d X'}{d \hat{\omega}} = - \sqrt{\frac{27}{16}} \left[\frac{\kappa' - (1 - \kappa') \hat{\omega} + \sqrt{8 \kappa' \hat{\omega}^3 + 3 \hat{\omega}^2}}{\hat{\omega}^{3/2}} \right], \quad (132)$$

$$\frac{d^2 X'}{d \hat{\omega}^2} = - \sqrt{\frac{27}{64}} \left[\frac{-3 \kappa' + (1 - \kappa') \hat{\omega} + 3 \hat{\omega}^2}{\hat{\omega}^{5/2}} \right]. \quad (133)$$

By analogy with the analysis of Sec. III C, we expect solutions of Eq. (131) for which $dX'/d\hat{\omega} < 0$ to be dynamically stable, and solutions for which $dX'/d\hat{\omega} > 0$ to be

dynamically unstable. This argument again leads to the conclusion that, when $\kappa' < \kappa'_c = 1/21.56$ (i.e., when the intrinsic plasma rotation is sufficiently high), the general solution of the torque-balance equation exhibits a “forbidden band” of island rotation frequencies. [Incidentally, the value of κ'_c is obtained from the simultaneous solution of $dX'/d\hat{\omega} = d^2X'/d\hat{\omega}^2 = 0$, with $dX'/d\hat{\omega}$ and $d^2X'/d\hat{\omega}^2 = 0$ given by Eqs. (132) and (133), respectively. At the critical point, $\hat{\omega} = \hat{\omega}_c = 1/9.198$ and $X' = X'_c = 1.795$.] This band separates a branch of dynamically stable low-frequency solutions from a branch of dynamically stable high-frequency solutions. As before, when a low-frequency solution crosses the lower boundary of the forbidden band, it becomes dynamically unstable, and there is (presumably) a bifurcation to a high-frequency solution (characterized by the same values of X' and κ'), and vice versa.

The critical values of X' and $\hat{\omega}$ where the aforementioned bifurcations take place, which are numerically determined from the solution of $dX'/d\hat{\omega} = 0$, with $dX'/d\hat{\omega}$ specified by Eq. (132), are shown in Figs. 7 and 8. It can be seen that, to a good approximation, there is a bifurcation from a high-frequency solution [i.e., $\hat{\omega} \sim \mathcal{O}(1)$] to a low-frequency solution [i.e., $\hat{\omega} \sim \mathcal{O}(\kappa')$] when X' exceeds the critical value

$$X'_+ \simeq 1 + \sqrt{6\kappa' + 164\kappa'^2}. \quad (134)$$

Just before the bifurcation, $\hat{\omega}$ takes the value

$$\hat{\omega}_+ \simeq \hat{\omega}_c + \left(\frac{1}{3} - \hat{\omega}_c\right) \sqrt{1 - \frac{\kappa'}{\kappa'_c}}. \quad (135)$$

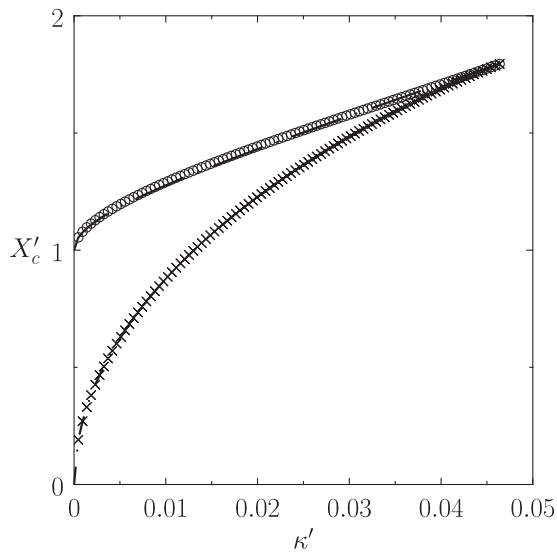


FIG. 7. Bifurcation thresholds derived from the thick-wall torque-balance equation. The circles show the critical X' value above which high-frequency solutions bifurcate to low-frequency solutions, plotted as a function of κ' . Similarly, the crosses show the critical X' value below which low-frequency solutions bifurcate to high-frequency solutions. The long-dashed-dotted curve shows the analytic approximation $X' = 1 + \sqrt{6\kappa' + 164\kappa'^2}$. The short-dashed-dotted curve shows the analytic approximation $X' = (1 + 1/\sqrt{2})\sqrt{27\kappa'(1 - \kappa' - 6.63\kappa'^2)}$.

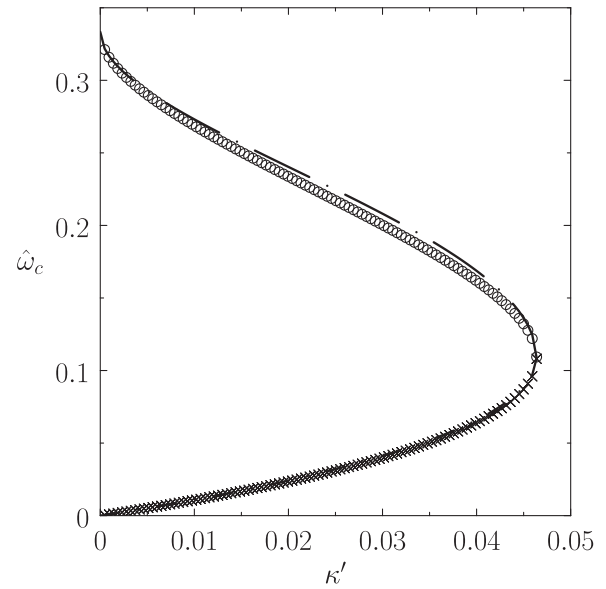


FIG. 8. Bifurcation thresholds derived from the thick-wall torque-balance equation. The circles show the critical $\hat{\omega}$ value at which high-frequency solutions bifurcate to low-frequency solutions, plotted as a function of κ' . Similarly, the crosses show the critical $\hat{\omega}$ value at which low-frequency solutions bifurcate to high-frequency solutions. The long-dashed-dotted curve shows the analytic approximation $\hat{\omega} = \hat{\omega}_c + (1/3 - \hat{\omega}_c)\sqrt{1 - \kappa'/\kappa'_c}$, where $\hat{\omega}_c = 1/9.198$ and $\kappa'_c = 1/21.56$. The short-dashed-dotted curve shows the analytic approximation $\hat{\omega} = \hat{\omega}_c - \hat{\omega}_c\sqrt{1 - 2(\kappa'/\hat{\omega}_c)(1 - \kappa'/\kappa'_c) - (\kappa'/\kappa'_c)^2}$.

On the other hand, there is a bifurcation from a low-frequency to a high-frequency solution when X' falls below the critical value

$$X'_- \simeq (1 + 1/\sqrt{2})\sqrt{27\kappa'(1 - \kappa' - 6.63\kappa'^2)}. \quad (136)$$

Just before the bifurcation, $\hat{\omega}$ takes the value

$$\hat{\omega}_- \simeq \hat{\omega}_c - \hat{\omega}_c\sqrt{1 - 2\left(\frac{\kappa'}{\hat{\omega}_c}\right)\left(1 - \frac{\kappa'}{\kappa'_c}\right) - \left(\frac{\kappa'}{\kappa'_c}\right)^2}. \quad (137)$$

Of course, Eqs. (134)–(137) are only valid when $\kappa' < \kappa'_c$. For $\kappa' \geq \kappa'_c$, there are no bifurcations, which implies that $\hat{\omega}$ varies smoothly and reversibly with X' . As before, the fact that $X'_- < X'_+$ suggests that the high-frequency/low-frequency bifurcation cycle exhibits considerable hysteresis. Note, incidentally, that Eqs. (134)–(137) are analytic approximations to the exact solutions (which cannot be expressed in closed forms).

D. Time-dependent solutions

Figure 9 shows a typical solution of the thick-wall rotation-braking equations (128) and (129), in which the island width parameter, X' , is very slowly (compared to the momentum confinement timescale) ramped up from zero to some maximum value that exceeds that at which the bifurcation from high-frequency to low-frequency solution branches is predicted to occur (according to torque-balance theory) and then very slowly ramped back down to zero. It can be seen that, at first, the normalized plasma rotation frequency, $\hat{\omega}$, decreases smoothly as X' increases. Eventually, however,

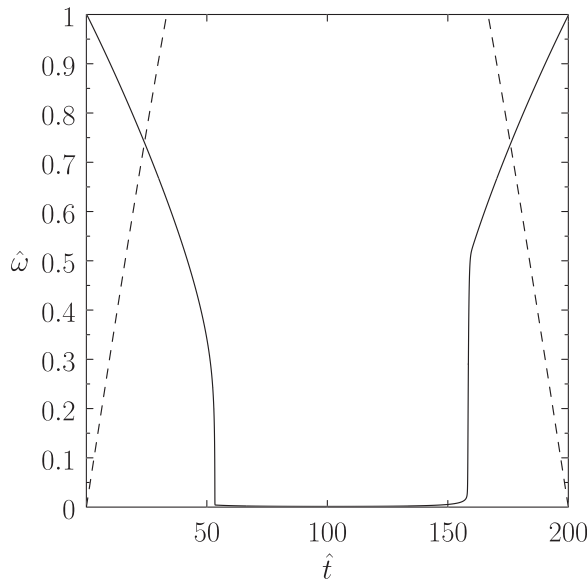


FIG. 9. Solution of the thick-wall rotation-braking equations, calculated with $\kappa = 0.02$, $\hat{r}_s = 0.5$, and $X = 2 \sin(\pi \hat{t}/200)$. The solid curve shows the normalized island rotation frequency, $\hat{\omega}$, plotted as a function of the normalized time. The dashed curve shows the imposed time variation of the island width parameter, X' .

when the rotation frequency has been reduced to about one third of its original value ($\hat{\omega} = 1$), the frequency drops precipitously to a very low value (compared to its original value.). This is the high-frequency to low-frequency bifurcation. Conversely, the rotation frequency initially rises smoothly, as X decreases, although it still takes a comparatively low value. Eventually, however, the frequency rises precipitously, attaining a value that is comparable with its original one. This is the low-frequency to high-frequency bifurcation. As before, the hysteresis in the high-frequency/low-frequency bifurcation cycle is illustrated by the strong asymmetry (about $\hat{t} = 100$) evident in the $\hat{\omega}$ - \hat{t} curve plotted in Fig. 9.

In the following, the start and end times of the high-to-low-frequency bifurcation are conveniently defined as the times at which $\Gamma \equiv |d\hat{\omega}/d\hat{t}|$ first exceeds the critical value 0.075, and subsequently first falls below this value, respectively. (Note that, except during the bifurcations, Γ is typically much smaller than 0.075.) The start and end times of the low-to-high-frequency bifurcation are defined in an analogous manner.

Figures 10 and 11 show the bifurcation thresholds (i.e., the values of X' and $\hat{\omega}$ at the start times of the high-to-low-frequency and low-to-high-frequency bifurcations) determined from the thick-wall rotation-braking equations, as a function of the parameter κ' . In all cases, $X'(t)$ is ramped up and down again, in the manner described in the caption to Fig. 9. Also, shown are the analytic approximations (134)–(137) that were previously derived from torque-balance theory. It is again clear that the analytic approximations are fairly accurate, which confirms, first, that torque-balance theory is capable of correctly predicting the occurrence of the high-to-low-frequency and low-to-high-frequency bifurcations, and, second, that solutions of the thick-wall torque-balance

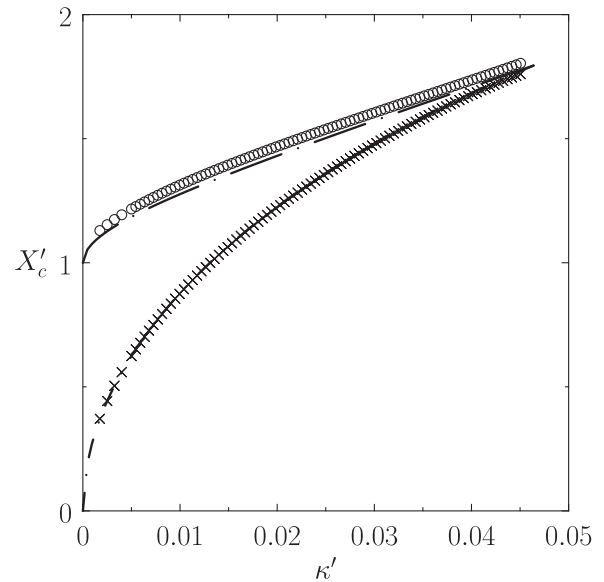


FIG. 10. Bifurcation thresholds derived from the thick-wall rotation-braking equations, with $\hat{r}_s = 0.5$. The circles show the critical X' value above which high-frequency solutions bifurcate to low-frequency solutions, plotted as a function of κ' . Similarly, the crosses show the critical X' value below which low-frequency solutions bifurcate to high-frequency solutions. The long-dashed-dotted curve shows the analytic approximation $X' = 1 + \sqrt{6\kappa' + 164\kappa'^2}$. The short-dashed-dotted curve shows the analytic approximation $X' = (1 + 1/\sqrt{2})\sqrt{27\kappa'(1 - \kappa' - 6.63\kappa'^2)}$.

equation characterized by $dX'/d\hat{\omega} > 0$ are indeed dynamically unstable.

As before, torque-balance theory is incapable of predicting the duration of a given bifurcation. Figure 12 shows the

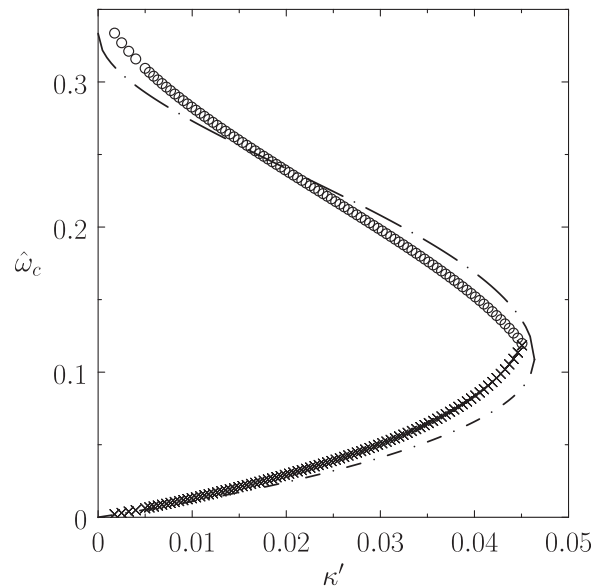


FIG. 11. Bifurcation thresholds derived from the thick-wall rotation-braking equations, with $\hat{r}_s = 0.5$. The circles show the critical $\hat{\omega}$ value at which high-frequency solutions bifurcate to low-frequency solutions, plotted as a function of κ' . Similarly, the crosses show the critical $\hat{\omega}$ value at which low-frequency solutions bifurcate to high-frequency solutions. The long-dashed-dotted curve shows the analytic approximation $\hat{\omega} = \hat{\omega}_c + (1/3 - \hat{\omega}_c)\sqrt{1 - \kappa'/\kappa'_c}$, where $\hat{\omega}_c = 1/9.198$ and $\kappa'_c = 1/21.56$. The short-dashed-dotted curve shows the analytic approximation $\hat{\omega} = \hat{\omega}_c - \hat{\omega}_c\sqrt{1 - 2(\kappa'/\hat{\omega}_c)(1 - \kappa'/\kappa'_c) - (\kappa'/\kappa'_c)^2}$.

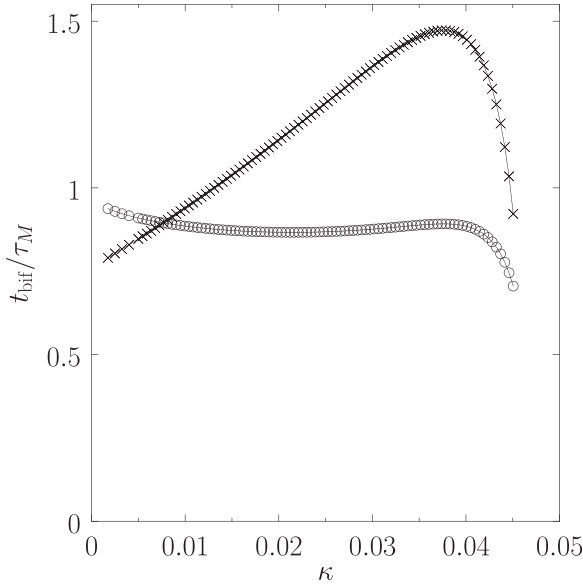


FIG. 12. Bifurcations times derived from the thick-wall rotation-braking equations, with $\hat{r}_s = 0.5$. The circles show the time required for the high-frequency to low-frequency bifurcation, plotted as a function of κ' . The crosses show the time required for the low-frequency to high-frequency bifurcation.

durations (i.e., the difference between the end and start times, as defined previously) of the high-to-low-frequency and low-to-high-frequency bifurcations determined from the thick-wall rotation-braking equations, as a function of the parameter κ' . Here, $X'(t)$ is ramped up and down again, in the manner described in the caption to Fig. 9. It is clear that, in order to reach completion, both types of bifurcations require a time interval whose duration is of order a momentum confinement time. Moreover, at small κ' , the low-to-high-frequency bifurcation is slightly faster than the high-to-low-frequency bifurcation, whereas the opposite is true at high κ' .

It is again apparent from the preceding discussion that [see Eq. (123)]

$$\left| \frac{d \ln \gamma}{dt} \right| \simeq \left| \frac{d \ln \omega}{dt} \right| \leq \frac{1}{\tau_M}. \quad (138)$$

Hence, the inequalities (126) yield

$$\omega_0 \tau_M, \omega_0 \tau_W \gg 1, \quad (139)$$

where τ_W is the timescale on which the island width varies. Furthermore, the inequality (66) reduces to

$$\tau_M \gg \left(\frac{\mu_w \tau_w}{\omega_0 \epsilon_w} \right)^{1/2}. \quad (140)$$

Finally, according to Eq. (122), the thick-wall regime only holds when (using $k \simeq m \mu_w$)

$$\omega_0 \tau_w \gg \frac{1}{\mu_w \epsilon_w}. \quad (141)$$

Thus, the previous three inequalities are the criteria for the validity of the theory presented in this section.

E. Effect of wall ferromagnetism

It follows from Eqs. (50), (57), (77), (118), (127), (134), and (136) that, in the thick-wall regime, the critical island width above which the high-to-low-frequency bifurcation is triggered can be written

$$W_+ \simeq \left\{ \left(\kappa'_c \frac{\lambda}{\lambda_c} \right)^{-1/2} \left[1 + \sqrt{6 \kappa'_c \frac{\lambda}{\lambda_c} + 164 \left(\kappa'_c \frac{\lambda}{\lambda_c} \right)^2} \right] \right\}^{1/4} W_3, \quad (142)$$

where

$$W_3 = \left[\frac{2^8 \sqrt{2}}{\sqrt{27}} \frac{\omega_0 \tau_H^2}{\tau_M} \frac{(q_s / \epsilon_a)^2}{m \ln(a/r_s)} \left(\frac{1}{\zeta} - \zeta \right) \right]^{1/4}, \quad (143)$$

$$\lambda_c = \kappa'_c \left(\frac{\omega_0 \tau_w}{m} \right) \left(\frac{1 - \zeta}{1 + \zeta} \right)^2, \quad (144)$$

and $\kappa'_c = 1/21.56$. Likewise, the critical island width below which the low-to-high-frequency bifurcation is triggered takes the form

$$W_- \simeq \left\{ \sqrt{27} \left(1 + \frac{1}{\sqrt{2}} \right) \left[1 - \kappa'_c \frac{\lambda}{\lambda_c} - 6.63 \left(\kappa'_c \frac{\lambda}{\lambda_c} \right)^2 \right] \right\}^{1/4} W_3. \quad (145)$$

Here, W_2 , λ , ω_0 , τ_w , m , and ζ are defined in Sec. III E.

There are bifurcations between high-frequency and low-frequency solution branches when λ , which parameterizes the degree of wall ferromagnetism, lies in the range $0 < \lambda < \lambda_c$. For $\lambda \geq \lambda_c$, there are no bifurcations, and the island frequency consequently varies smoothly and reversibly as the island width varies. According to Eq. (122), the thick-wall ordering is only valid provided

$$\lambda \gg \frac{\kappa'_c}{\lambda_c} \left(\frac{1 - \zeta}{1 + \zeta} \right)^2. \quad (146)$$

Thus, in order to have bifurcations in the thick-wall regime, we require

$$\lambda_c \gg \sqrt{\kappa'_c} \left(\frac{1 - \zeta}{1 + \zeta} \right) \simeq 0.21 \left(\frac{1 - \zeta}{1 + \zeta} \right). \quad (147)$$

This criterion is easily satisfied provided that $\omega_0 \tau_w$ is sufficiently large (i.e., provided that the intrinsic plasma rotation is sufficiently large).

Figure 13 shows W_+/W_3 and W_-/W_3 plotted as functions of λ/λ_c . It can be seen that, for $\lambda \ll \lambda_c$, increasing wall ferromagnetism (i.e., increasing λ) causes a marked decrease in W_+ , but leaves W_- virtually unaffected. In other words, ferromagnetism significantly reduces the critical island width above which a rotating tearing mode “locks” to the wall, but makes little difference to the critical width below which the mode “unlocks.” On the other hand, W_+ asymptotes to W_- (which remains essentially independent of λ) from above as $\lambda \rightarrow \lambda_c$. Of course, there are no

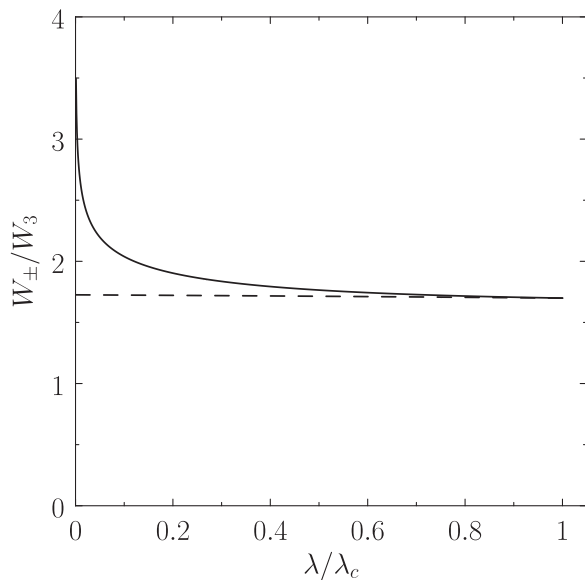


FIG. 13. Bifurcation thresholds in the thick-wall regime. The solid curve shows the critical island width (normalized to W_3) above which high-frequency solutions bifurcate to low-frequency solutions, plotted as a function of the wall ferromagnetism parameter, λ/λ_c . Similarly, the dashed curve shows the critical island width below which low-frequency solutions bifurcate to high-frequency solutions.

bifurcations for $\lambda \geq \lambda_c$. Hence, increasing wall ferromagnetism eventually suppresses the bifurcations, in which case the island rotation frequency varies smoothly and reversibly with the island width.

V. SUMMARY

This paper contains an in-depth investigation of the braking of tearing mode rotation in tokamak plasmas via eddy currents induced in external conducting structures. The analysis is subject to a number of limitations. First, it only applies to large-aspect ratio, low- β , circular cross-section, tokamak plasmas. Second, it assumes that the tearing mode amplitude varies on a timescale that is much longer than the plasma momentum confinement timescale. Third, it assumes that the plasma density and perpendicular viscosity are uniform across the plasma. Fourth, it assumes that the plasma poloidal rotation profile is fixed due to the action of strong poloidal flow damping. Fifth, it neglects the transient response of the eddy currents to the magnetic field generated by the rotating tearing mode. Finally, it assumes that the conducting structure, or “wall,” is of uniform thickness, resistivity, and magnetic permeability, is physically thin (i.e., its radial thickness is much less than its minor radius), and concentric with the plasma.

As is well-known,¹⁰ for sufficiently large intrinsic plasma rotation, there is a “forbidden band” of tearing mode rotation frequencies that separates a branch of high-frequency solutions from a branch of low-frequency solutions. When a high-frequency solution crosses the upper boundary of the forbidden band, there is a bifurcation to a low-frequency solution, and vice versa. There is considerable hysteresis in this process, because the critical tearing mode amplitude above which the high-frequency to low-

frequency bifurcation is triggered is much larger than the critical mode amplitude below which the opposite bifurcation is triggered.

The aims of this paper were threefold. First, to verify that the bifurcation thresholds predicted by simple torque-balance theory (which takes into account the electromagnetic braking torque acting on the plasma, and well as the plasma viscous restoring torque, but neglects plasma inertia) are the same as those predicted by more complicated time-dependent mode braking theory (which takes inertia into account). This was, indeed, found to be the case (see Secs. III D and IV D). Second, to generalize existing theory to allow for electromagnetically thick conducting structures. This was achieved in Sec. IV. Finally, to generalize the theory to allow the conducting structures to be ferromagnetic. The results of this generalization are described in Secs. III E and IV E. It is found that significant ferromagnetism causes otherwise electromagnetically thin conducting structures to become electromagnetically thick, and also markedly decreases the critical tearing mode amplitude above which the mode “locks” to the conducting structures (i.e., the high-frequency to low-frequency bifurcation is triggered). On the other hand, if the ferromagnetism becomes too large, then the forbidden band of mode rotation frequencies is suppressed, and the mode frequency consequently varies smoothly and reversibly with the mode amplitude.

ACKNOWLEDGMENTS

This research was funded by the U.S. Department of Energy under Contract No. DE-FG02-04ER-54742.

- ¹J. A. Wesson, *Tokamaks*, 4th ed. (Oxford University Press, Oxford, 2012).
- ²J. P. Freidberg, *Ideal Magnetohydrodynamics* (Springer, Berlin, 1987).
- ³J. A. Wesson, *Nucl. Fusion* **18**, 87 (1978).
- ⁴H. P. Furth, J. Killeen, and M. N. Rosenbluth, *Phys. Fluids* **6**, 459 (1963).
- ⁵P. H. Rutherford, *Phys. Fluids* **16**, 1903 (1973).
- ⁶A. Thyagaraja, *Phys. Fluids* **24**, 1716 (1981).
- ⁷D. F. Escande and M. Ottaviani, *Phys. Lett. A* **323**, 278 (2004).
- ⁸R. J. Hastie, F. Militello, and F. Porcelli, *Phys. Rev. Lett.* **95**, 065001 (2005).
- ⁹Z. Chang and J. D. Callen, *Nucl. Fusion* **30**, 219 (1990).
- ¹⁰R. Fitzpatrick, *Nucl. Fusion* **33**, 1049 (1993).
- ¹¹T. C. Hender, C. G. Gimblett, and D. C. Robinson, *Nucl. Fusion* **29**, 1279 (1989).
- ¹²G. Berge, L. K. Sandal, and J. A. Wesson, *Phys. Scr.* **40**, 173 (1989).
- ¹³M. F. F. Nave and J. A. Wesson, *Nucl. Fusion* **30**, 2575 (1990).
- ¹⁴H. Zohm, A. Kallenbach, H. Bruhns, G. Fussmann, and O. Klüber, *Europhys. Lett* **11**, 745 (1990).
- ¹⁵B. E. Chapman, R. Fitzpatrick, D. Craig, P. Martin, and G. Spizzo, *Phys. Plasmas* **11**, 2156 (2004).
- ¹⁶J. A. Snipes, D. J. Campbell, P. S. Haynes, T. C. Hender, M. Hugon, P. J. Lomas, N. J. Lopes Cardozo, M. F. F. Nave, and F. C. Schüller, *Nucl. Fusion* **28**, 1085 (1988).
- ¹⁷P. C. de Vries, M. F. Johnson, B. Alper, P. Buratti, T. C. Hender, H. R. Koslowski, V. Riccardo, and JET-EFDA Contributors, *Nucl. Fusion* **51**, 053018 (2011).
- ¹⁸D. A. Gates and T. C. Hender, *Nucl. Fusion* **36**, 273 (1996).

- ¹⁹R. Aymar, P. Barabashchi, and Y. Shimomura, *Plasma Phys. Controlled Fusion* **44**, 519 (2002).
- ²⁰C. Gimblett, *Nucl. Fusion* **26**, 617 (1986).
- ²¹W. F. Bergerson, D. A. Hannum, C. C. Hegna, R. D. Kendrick, J. S. Sarff, and C. B. Forest, *Phys. Rev. Lett.* **101**, 235005 (2008).
- ²²J. P. Levesque, P. E. Hughes, J. Bialek, P. J. Byrne, M. E. Mauel, G. A. Navratil, Q. Peng, D. J. Rhodes, and C. C. Stofer, *Phys. Plasmas* **22**, 056102 (2015).
- ²³M. Tamura, H. Hayakawa, A. Yoshitake, A. Hishinuma, and T. Kondo, *J. Nucl. Mater.* **155–157**, 620 (1988).
- ²⁴R. Fitzpatrick and E. P. Yu, *Phys. Plasmas* **6**, 3536 (1999).
- ²⁵R. Fitzpatrick, R. J. Hastie, T. J. Martin, and C. M. Roach, *Nucl. Fusion* **33**, 1533 (1993).
- ²⁶S. C. Guo and M. S. Chu, *Phys. Plasmas* **9**, 4685 (2002).
- ²⁷R. Fitzpatrick, *Phys. Plasmas* **21**, 092513 (2014).
- ²⁸R. Fitzpatrick, *Phys. Plasmas* **5**, 3325 (1998).